Optimization of a Quasi-Mesh Absorber for the Terahertz Intensity Mapper

Rong Nie, Reinier M. J. Janssen, Charles M. Bradford, Jeffrey P. Filippini, and Steven Hailey-Dunsheath

***Abstract*—We discuss the design and optimization of the absorber for the long-wavelength arm of the Terahertz intensity mapper, a balloon-borne spectrometer employing kinetic inductance detectors. Electromagnetic simulations of our design indicate in-band absorption efficiency over $\sim 80\%$ in both linear polarization modes. By developing custom transmission line model and mode-matching calculations, we find the absorption efficiency is affected by the absorber's reactive part and overall shape. These insights into the operation of this design provide guidance for its optimization for low-resistance absorber materials.**

***Index Terms*—Electromagnetic simulations, kinetic inductance detector (KID), mode matching (MM) method, Terahertz intensity mapper (TIM), transmission line theory.**

I. Introduction

UNDERSTANDING the history of star formation throughout cosmic time would provide significant insights into the processes of galactic evolution. The far-infrared (FIR) wavelength band contains valuable information to address this question: half of the total energy output from the cosmic star formation has been absorbed by interstellar dust and reemitted in the FIR [1] and [2]. Un-extincted FIR spectral lines (e.g., [CII], [NII], [OI]) can reveal the composition of the interstellar medium (ISM) and the abundance of star-forming clouds. Traditional single-object observations suffer from limitations of individual galaxy brightness, angular resolution, and survey speed. Line intensity mapping (LIM) is an emerging technique that maps the *integrated* emission of spectral lines from galaxies [3], which appear at different wavelengths depending on the redshifts of their sources. LIM thus enables study of the ISM and galaxy evolution over cosmic time without demanding high-angular resolution [4].

The low noise, broad bandwidth, and large survey area required for FIR LIM demands an observing platform above the bulk of the Earth's atmosphere. The Terahertz intensity mapper (TIM) [5] is a balloon-borne FIR spectrometer designed to observe key spectral line tracers at the epoch of peak cosmic star formation. With an observing bandwidth of 240–420 μm, TIM will observe spectral lines from [CII] (158 μm, visible $0.5< z <1.6$), [NII] (205 μm, $0.2< z <1$), [OI] (63 μm, $2.8< z <5.7$), and [OIII] (88 μm, $1.7< z <3.8$), spanning the crucial gap in spectroscopic coverage between the Atacama Large Millimeter Array (ALMA) and the James Webb Space Telescope (JWST). TIM will make a pioneering demonstration of LIM by observing both *spectral* and *spatial* signals. In addition, TIM will: first, detect $\sim$100 galaxies to constrain models of galaxy evolution; second, capture the star formation contribution of galaxies too faint to be detected individually through the measurement of the [CII] luminosity function across the peak of cosmic star formation; third, stack [CII] and [NII] lines on stellar mass-selected galaxies with spectroscopic redshifts, informing theory to relate this to the total star formation rate, star formation mode, metallicity, and specific star formation rate; and finally, measure the specific star formation rate as a function of redshift by cross-correlation with data from the Herschel and Spitzer space telescopes. Moreover, TIM will be a vital technological and scientific stepping stone to future orbital missions such as the Origins Space Telescope [6].

The promise of FIR LIM brings with it substantial technical challenges. TIM's 2 m warm reflector will feed an $R \sim 400$ grating spectrometer, partitioned into long wavelength (LW: 317–420 μm) and short wavelength (SW: 240–317 μm) modules. To approach photon-noise-limited performance with high scalability, TIM employs feedhorn-coupled aluminum kinetic inductance detector (KID) arrays operated at 250 mK [7]. These KIDs will employ a lithographically patterned aluminum absorber coupled to a waveguide to absorb the incoming radiation.

In this article, we discuss electromagnetic simulation results and optimization studies for a TIM absorber design based upon that used in the MAKO camera [8]. We further try to give greater intuition for our results using two approaches: transmission line theory and the mode-matching (MM) method.

Manuscript received June 1, 2020; revised August 11, 2020; accepted August 24, 2020. Date of publication September 4, 2020; date of current version November 3, 2020. This work was carried out as part of the Terahertz Intensity Mapper project, supported by NASA under Grant 80NSSC19K1242, issued through the Science Mission Directorate. The work of Reinier M. J. Janssen was supported by an appointment to the NASA Postdoctoral Program at the NASA Jet Propulsion Laboratory, administered by Universities Space Research Association under contract with NASA. This research was carried out in-part at the Jet Propulsion Laboratory, California Institute of Technology, under a contract with the National Aeronautics and Space Administration (80NM0018D0004). *(Corresponding author: Rong Nie.)*

Rong Nie and Jeffrey P. Filippini are with the Department of Physics, University of Illinois at Urbana-Champaign, Urbana, IL 61801 USA (e-mail: rongnie2@illinois.edu; jpf@illinois.edu).

Reinier M. J. Janssen and Charles M. Bradford are with Jet Propulsion Laboratory, California Institute of Technology, Pasadena, CA 91109 USA, and also with the Department of Astronomy, California Institute of Technology, Pasadena, CA 91125 USA (e-mail: rjanssen@jpl.nasa.gov; bradford@submm.caltech.edu).

Steven Hailey-Dunsheath is with the Department of Astronomy, California Institute of Technology, Pasadena, CA 91125 USA (e-mail: haileyds@caltech.edu).

Color versions of one or more of the figures in this article are available online at https://ieeexplore.ieee.org.

Digital Object Identifier 10.1109/TTHZ.2020.3022020

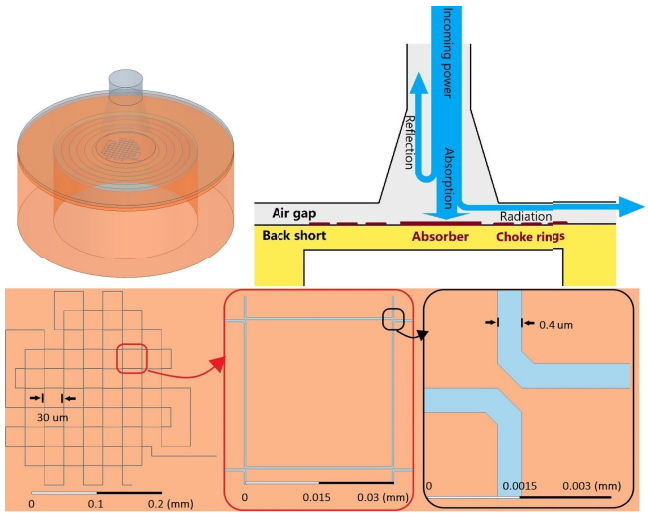

Fig. 1. *Top*: 3-D rendering in HFSS and side view cartoon of a single pixel. Photons propagate from the top port through a flared circular waveguide onto the aluminum meander, which is front-side illuminated and surrounded by three optical choke rings. A back-short layer is deposited on the other side of the silicon wafer. *Bottom*: Top view of the meander geometry, with insets highlighting mesh intersections. The various segments of meander line come close enough to one another at the corners to create capacitive shorts at the optical frequencies. The *Bottom Middle* panel is effectively a unit cell of the entire absorber. Throughout this article, x and y refer to the vertical and horizontal axes of the lower pane.

II. Finite-Element Simulations

Inspired by the design developed for MAKO, the proposed TIM absorber (Fig. 1) is a 30 nm thick and 400 nm wide aluminum (Al) meandering line forming a quasi-mesh structure, patterned onto a silicon wafer with integrated back-short. The MAKO absorber was developed for the high sheet resistance, R_s, of titanium nitride (TiN) KIDs. While TiN is well suited to high-loading applications such as ground-based imaging [9], or low-volume applications such as a microstrip-coupled on-chip spectrometer [10], [11], the properties of this disordered superconductor do not allow it to reach the sensitivities required for TIM when patterned into an absorbing structure [12]. A key challenge for TIM is thus to adapt this design to the much lower resistivity ($R_{s\mathrm{TiN}}/R_{s\mathrm{Al}} \sim 100$) of aluminum, which is the material of choice for low-loading applications [13].

Building off an initial design [7], we carried out a program of simulations using the finite-element method (FEM) electromagnetic software ANSYS-high-frequency structure simulator (HFSS). Fig. 1 shows the simulation setup. Radiation is guided to the quasi-mesh absorber by a 127 μm radius circular waveguide that flares out to a 225 μm radius near the absorber. The waveguide and absorber are separated by a short air gap. The absorber is located on a Si wafer with a metalized backside, which functions as a $\lambda/4$ back-short. In addition, the front-side illuminated absorber is surrounded by three aluminum choke rings. In the optimized design the air gap and back-short distances are 25 and 27 μm, respectively. Both the choke ring widths and the gaps between them are 58 μm.

Power is propagated down the waveguide in the TE_{11} mode, since this is the only mode carried by the waveguide over a large part of the frequency band; the lowest three cutoff frequencies for a circular waveguide with radius $a = 127$ μm are $\mathrm{TE}_{11} = 691.6$ GHz, $\mathrm{TM}_{01} = 903.6$ GHz, and $\mathrm{TE}_{21} = 1147.4$ GHz. The incoming power from the waveguide is distributed to five different ports, each measured independently in HFSS: absorption by the antenna (P_{ab}), reflection back to the waveguide ($|S_{11}|^2$), absorption by the choke rings (P_{cr}), and radiation escaping the pixel through the air gap (P_{ag}) and the substrate (P_{sb}). The reflected power comes from S_{11} directly, while the absorbed and radiated powers are defined as $P_i = \int \mathrm{Re}(\mathbf{S} \cdot \mathbf{n}) dA_i$, where $\mathbf{S}$ is the Poynting vector, and $\mathbf{n}$ is the unit outward normal vector of each surface A_i. As a consistency check, we computed the sum of these five components to confirm that they match the input power to $<0.1\%$. Further details are given in the appendix.

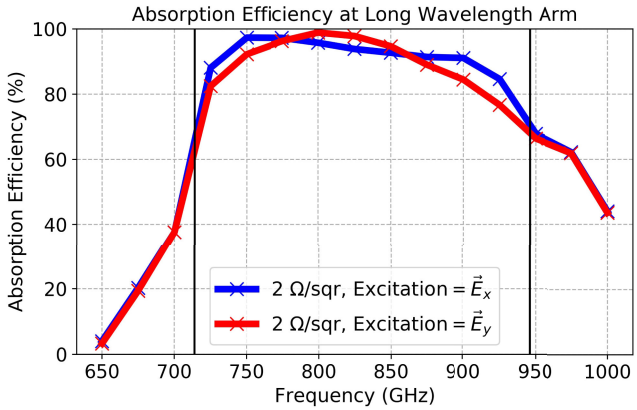

Fig. 2. Simulation results for the LW optimized design: air gap distance $=$ 25 μm, back-short distance $=$ 27 μm, line width $=$ 0.4 μm, the waveguide is excited by a single circular TE_{11} mode, and the absorber is surrounded by three choke rings. Vertical lines delimit the desired bandwidth (714–946 GHz).

We optimized over the following parameters: (a) air gap and (b) back-short distances, (c) meandering line width, and (d) total absorber size. We also explored the effects of (e) including higher order circular waveguide modes, (f) switching to a rectangular waveguide, (g) excluding the choke structures, and (h) changing the choke ring dimensions.

Fig. 2 shows the absorption efficiency of the optimized design. Absorption at low frequencies is suppressed by the waveguide cutoff frequency, while the high frequencies are reduced by the back-short thickness. Since TIM's detectors should ideally be sensitive to incoming signals independent of polarization, we investigate antenna performance in both x and y polarizations (blue and red lines in Fig. 2). We also simulate a representative input signal polarized at an intermediate angle and with an arbitrary phase delay ($E_{in} = \vec{E_x} + e^{0.28\pi i}\vec{E_y}$); the result is similar to the simple superposition of polarizations, suggesting that the independent study of x and y-polarization performance shown here is adequate.

Simulated variations of (c), (d), (e), and (h) show that the current configuration is optimal. A rectangular waveguide with similar cutoff frequencies (f) results in lower absorption efficiency at both polarizations. Removing the choke rings (g) results in $\sim 10\times$ higher power leakage through the air gap and back-short wafer but only a marginal change in absorption

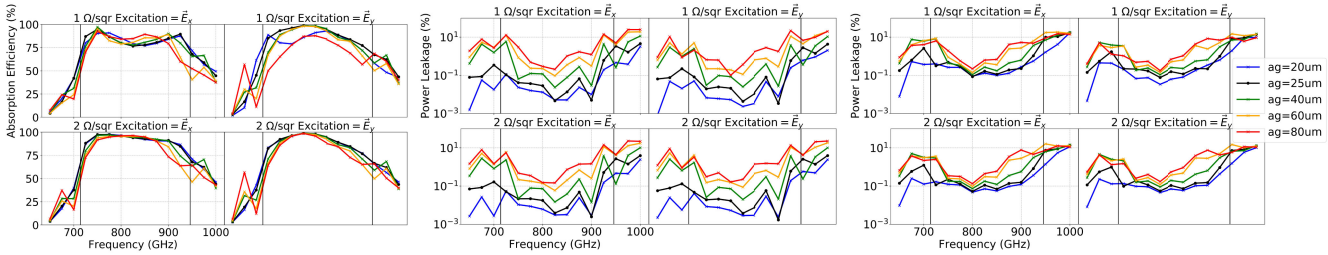

Fig. 3. *Left*: Absorption efficiency under variation of air gap (ag) distance. Black lines indicate the current design with air gap $= 25\mu$m. *Middle and right*: Power leakage through air gap and wafer, respectively.

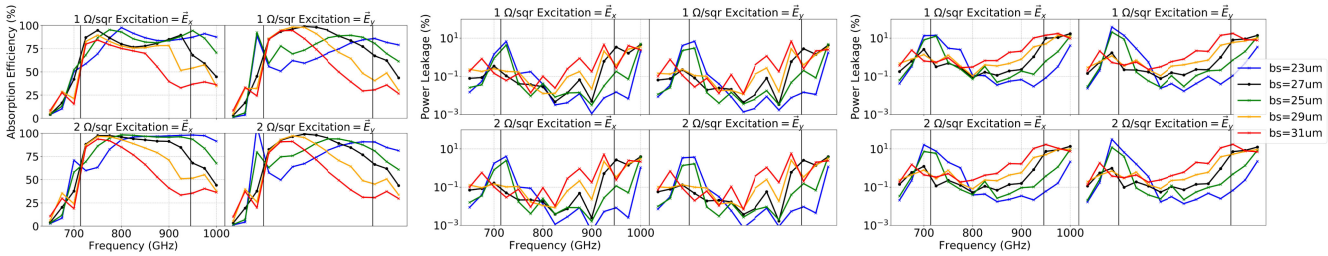

Fig. 4. *Left*: Absorption efficiency under variation of back-short (bs) thickness. Black lines indicate the current design with back-short $= 27\mu$m. *Middle and right*: Power leakage through air gap and wafer, respectively.

efficiency, suggesting that this power is otherwise reflected back into the waveguide. Figs. 3 and 4 show the simulated response to variation of the (a) air gap distance (ag, from 20 to 80 μm), and (b) back-short thickness (bs, from 23 to 31 μm), respectively, for two choices of sheet resistance ($R_s = 1$ or $2\Omega/\square$). For each of these parameters, we examine the absorption efficiency of the antenna and the power leakage through the air gap and substrate; the latter contribute to possible optical crosstalk among channels. Fig. 3 indicates that increasing the air gap produces larger power leakage; within the 20–80 μm range, the effect can be as large as a factor of 10. The power leakage benefits of air gaps $< 25\ \mu$m are minimal; in particular, leakage through the air gap ($\sim$0.1%) remains well below optical crosstalk requirements ($<$1%). In addition, since the air gap separates the KID metal layer from a ground (the horn block), a touch can result in anything from a few dead pixels to a damaged array. Based upon practical experience with fabrication tolerances and horn block deformation during cooldown, TIM has set a lower limit of 30 μm on the air gap, with a desired value $\geq$50 μm. Fig. 4 shows a strong effect of the back-short distance on the absorption efficiency. Increasing the back-short distance moves the peak absorption efficiency to longer wavelengths (lower frequencies) and vice versa, as well as subtly affecting the power leakage. From these two studies we determine that the presented design results in an antenna efficiency $\sim 80\%$ across the band and a total power leakage at the 0.1% level. This study also shows wafer thickness (i.e., back-short spacing) to be a critical performance parameter for this design.

FEM simulation results may be sensitive to the number or size of the meshed elements, especially in a model with fine structure. The maximum number of meshed elements is constrained by the memory of the computing resource, however, making it challenging to run extremely fine meshed simulations on a large set of complete models (Fig. 1 upper left). An alternate method to probe this effect is to simulate a unit cell of the quasi-mesh pattern that forms the bulk of the absorber (Fig. 1 lower middle) with periodic boundary conditions, as described further in Section III-A. This method should capture the lowest-order behavior of the antenna, and allows access to meshes up to $10\times$ finer than those of the full simulations. Fig. 5 shows the results of varying the mesh density in this unit cell model: the dependence on the number of meshed elements is weak and nonmonotonic, suggesting that the coarser (but adaptive) mesh used in the full simulations captures the antenna's behavior with good fidelity.

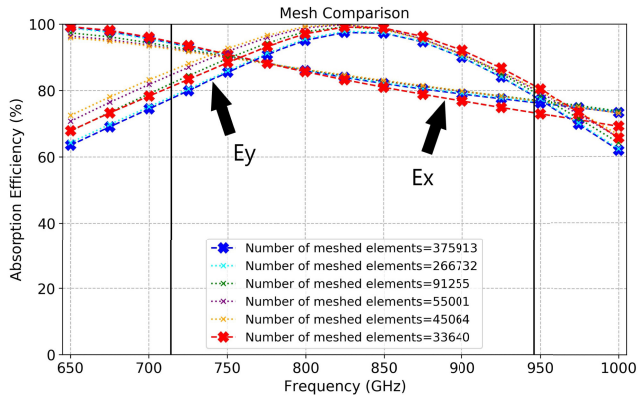

Fig. 5. Comparison of absorption efficiencies for the unit cell model, computed using different simulation mesh parameters. Arrows indicate curves for x and y polarizations. The bold red marks and the full scale simulations (e.g., Fig. 2) have the same adaptive mesh density in HFSS.

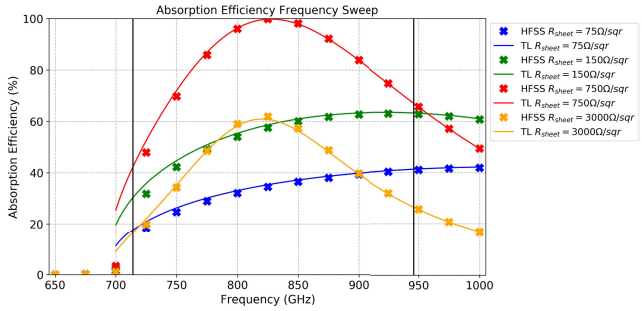

Fig. 6. Absorption efficiency for the model shown in Fig. 7. Cross markers are HFSS simulation results, and solid lines are TL theory. They are in good consistency, with some difference occurring when the frequency is close to the cutoff frequency. Green curve shows a sheet resistance of $150\,\Omega/\square$ results in an absorption efficiency of $\sim$50%.

We intend to employ a more powerful computing cluster in future work, but note that the coarse meshing allows rapid initial exploration of phase space. Additionally, comparison of Figs. 5 and 2 shows that the unit cell technique offers a useful approximation to the full waveguide simulation; it captures the "flat" and "concave" features for x and y polarizations.

III. Simplified Absorption Models

Although the simulations abovementioned show good results for the optimized design, it is notable that the calculated absorption efficiency is much higher than we might expect from considerations of impedance matching. At the center of our frequency band, the impedance of the waveguide is $\sim$700 Ω while the effective sheet resistance of the antenna is $2 \times 75 = 150\,\Omega/\square$ (where the area-filling fraction of the absorber is 1/75). We would thus naively expect an absorption efficiency of $\sim$50% rather than $\sim$90% in a simple transmission line (TL) model. Fig. 6 illustrates this contrast: red curves are matched impedance at $\sim$750 $\Omega/\square$, green curves are mismatched $\sim$ 150$\Omega/\square$ absorber resistance. This model does not account for the 25 μm air gap, but as this distance is small compared with the wavelength in the waveguide at this frequency ($\sim$650 μm) its impact should be modest. Below we develop illustrative qualitative models to explore this "anomaly". These models provide useful intuition for tuning absorber performance and informing future designs, as well as saving the computational expense of sweeping over a large parameter space in FEM simulations.

We can approach this problem in two ways. In the *microscopic* picture, we model the absorber as an array of identical unit cells filling the input waveguide, and use the unit cell impedance to analyze the equivalent circuit in a *TL model* [14]. In the *macroscopic* picture, we instead model the absorber as a two-dimensional (2-D) resistive sheet partially filling the waveguide and vary absorber properties using a custom *MM method* [15] code. Both models are implemented in custom Python code.

A. TL Theory

Consider a circular waveguide terminated by a thin-film coating, silicon-filled back-short, as shown at left in Fig. 7.

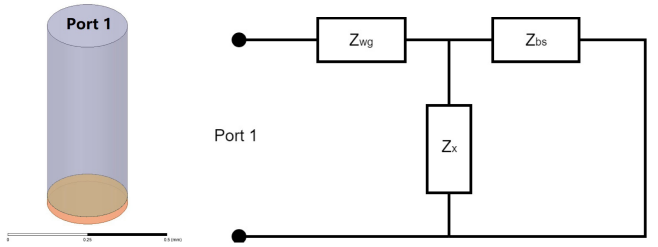

Fig. 7. *Left*: 3-D rendering of a simple model. From top to bottom, there is an input port, circular waveguide filled with vacuum, thin-film, circular waveguide filled with silicon. Note that the side and bottom boundaries set to perfect conductors. *Right*: Equivalent TL model.

The equivalent impedance model is shown in the right-hand panel, with $Z_{\rm wg}$, Z_x, and $Z_{\rm bs}$ representing the impedances of the waveguide, film, and back-short, respectively. The absorbed power A in the film is then given by

$$A = 1 - |S_{11}|^2 \tag{1}$$

where

$$S_{11} = \frac{Z_1 - Z_{\rm wg}}{Z_1 + Z_{\rm wg}} \tag{2}$$

$$Z_1 = \frac{Z_x Z_{\rm bs}}{Z_x + Z_{\rm bs}} \tag{3}$$

$$Z_{\rm bs} = jZ_{\rm wgbs} \tan\left(\frac{2\pi l_{\rm bs}}{\lambda_{\rm bs}}\right) \tag{4}$$

$l_{\rm bs}$ is the back-short thickness, and $\lambda_{\rm bs}$ is the wavelength within the silicon back-short. To write down A explicitly, we need to know $Z_{\rm wg}$ and $Z_{\rm wgbs}$, which are the impedances of the waveguide filled with vacuum and silicon, respectively. For a circular waveguide with TE$_{nm}$ modes [16],

$$Z_{\rm TE} = \frac{k\eta}{\beta} = \frac{\omega\mu}{\beta}. \tag{5}$$

In (5), $k = 2\pi/\lambda = \omega\sqrt{\epsilon\mu} = \omega/v$ is wave number, λ is wavelength, $\omega = 2\pi f$ is angular frequency, v is wave speed, and ϵ and μ are material permittivity and permeability, respectively. β is the propagation constant defined by

$$\beta = \sqrt{k^2 - k_c^2} = \sqrt{k^2 - (p'_{nm}/a)^2} \tag{6}$$

where a is the waveguide radius, k_c is the cutoff wave number, and p'_{nm} is the mth root of J'_n (the derivative of the Bessel function of first kind J_n with respect to its argument).

The lowest three cutoff frequencies for a waveguide with radius $a = 127$ μm are TE$_{11}$ = 691.6 GHz, TM$_{01}$ = 903.6 GHz, and TE$_{21}$ = 1147.4 GHz. We consider the TE$_{11}$ mode here as an example of the TL analysis. For a back-short thickness of $l_{\rm bs} = 27$ μm the quarter-wavelength condition is satisfied at 829.3 GHz, and for a purely resistive sheet we should achieve 100% absorption when $R_{\rm sheet} = Z_{\rm wg} = 682.8\,\Omega/\square$. Fig. 6 shows good consistency between TL theory and HFSS simulation, with significant discrepancy only near the waveguide cutoff. With our actual $R_{\rm sheet} = 75$ or $150\,\Omega/\square$ (1 or $2\Omega/\square$ Al sheet resistance with a filling factor of 1/75), the mismatch is severe and the absorption efficiency is low.

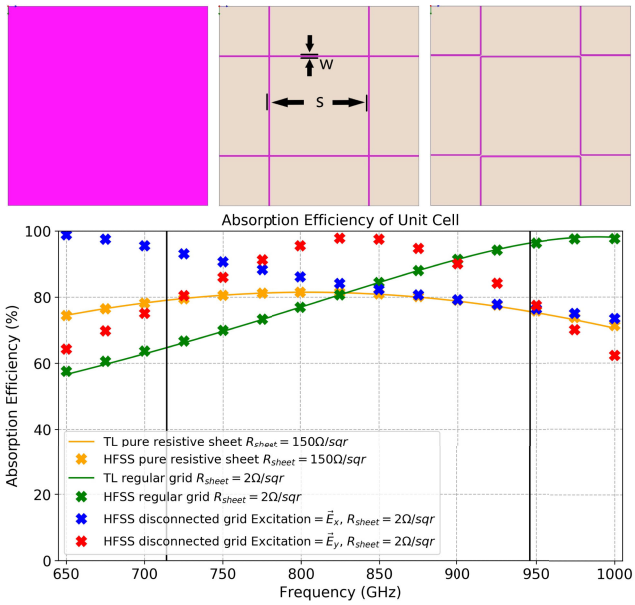

Fig. 8. Illustration of the unit cell analysis. *Upper* from left to right, the three absorber geometries considered: a purely resistive sheet; a continuous grid with connected vertices and periodic boundary conditions; and the actual absorber grid with disconnected vertices. *Lower*: Comparison between TL model based on (7) and FEM simulations. Orange cross markers and curves are results from HFSS and TL for the purely resistive sheet, respectively. Green cross markers and curves are results from HFSS and TL for the continuous grid, respectively. In these cases HFSS and the TL model are in good agreement. The resistive sheet and continuous grid are not polarization dependent. For a discontinuous grid, only the HFSS simulation is available. This geometry breaks the x and y symmetry. The shift in peak absorption frequency also suggests a further increase of the reactive part of the impedance with respect to the continuous grid.

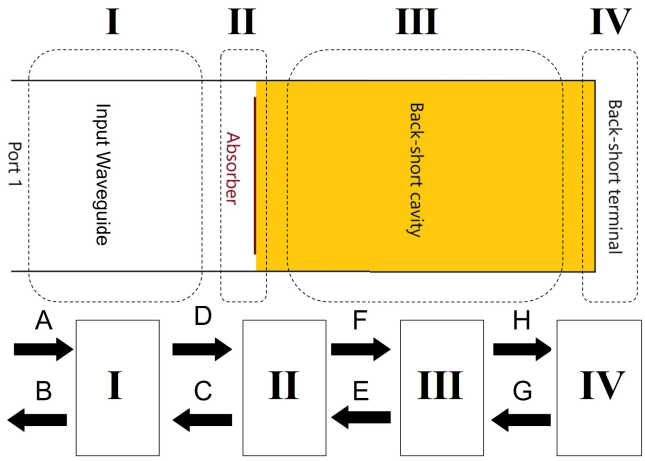

Fig. 9. Illustration of the key components of the MM model. *Upper*: Components of the waveguide termination model (*not to scale*). Note that regions II and IV represent thin 2-D layers, with no z-axis extent. Shading represents silicon. *Lower*: Model schematic, showing the cascaded matrices (I, II, III, IV) and input and output fields (*arrows*).

This discrepancy with FEM simulations (Fig. 2) suggests that this model is too simple. Our next step is to model the absorber as a continuous square metal grid, with the same line width and spacing as the real absorber but connected vertices. The upper panel of Fig. 8 compares a single unit cell of such a simplified grid with a unit of the real absorber. The following equation is valid when $w \ll s < \lambda$ [14]:

$$Z_x = R_{\text{eff}} + j\omega L = \frac{sR_{\text{sheet}}}{w} + j\omega\frac{sZ_{\text{wg}}}{2\pi v}\ln\left(\csc\left(\frac{\pi w}{2s}\right)\right). \tag{7}$$

In our case, line width $w = 0.4\ \mu$m and spacing $s = 30\ \mu$m. This captures the fact that our design takes advantage of the factor of s/w in (7) to boost the geometric effective sheet resistance R_{eff} abovementioned that of the low-resistivity material itself ($\sim 2\ \Omega/\square$) for better impedance matching. Note that we can no longer treat the absorber as purely resistive – the mesh geometry generates an inductive component.

To investigate the effect of the absorber's added reactive component, we simulate a unit cell of the absorber in HFSS. In top view our simulation is a square of side 2 s, with periodic boundary conditions imposed on the four vertical walls and the same vertical (z-direction) material stack shown in Fig. 7 (*left*). The absorber unit cell in this simulation is chosen to be either a uniform resistive sheet matching the effective absorber sheet resistance ($150\,\Omega/\square$), a continuous grid with an area-filling fraction matching the quasi-mesh absorber, or a unit cell of the actual quasi-mesh absorber as shown in the bottom middle panel of Fig. 1.

Fig. 8 bottom shows the results of this unit cell analysis. It is clear that the impedance of the mesh (green) is not purely resistive (orange). The lines of the mesh add a reactive (inductive) part to the impedance, which increases $|Z|$ toward the resonance frequency (~ 1 THz for the continuous grid). The presence of narrow gaps at the mesh vertices (as present in the actual absorber) adds additional capacitance, which reduces the frequency of maximum absorption. In addition, the disconnected vertices break symmetry and introduce polarization dependence to the absorption efficiency.

Note that, in contrast to other simulations presented in this article, the unit cell simulation uses periodic boundary conditions and Floquet port excitation. As a result of these new boundary conditions the input wave differs significantly from that of the actual waveguide – in the unit cell simulations we are effectively simulating plane waves in free space, with $Z_{\text{wg}} = 377\,\Omega$ (the free space impedance). This explains the much higher absorption efficiency of a pure resistive sheet at $150\,\Omega/\square$ (orange curve and markers on Fig. 8 lower plot) relative to Fig. 6 (green curve and markers).

B. MM Method

In addition to the microscopic understanding given by the TL and unit cell analyses, the absorber's efficiency also depends upon its overall profile, in particular its size with respect to that of the waveguide. To study this macroscopic behavior, we employ the MM method [15]. The principal insight is that, because the absorber is approximately a 2-D metal layer coupled to a waveguide, we can expand the electromagnetic field in any plane as a sum of waveguide modes. By imposing the scattering matrix and proper boundary conditions at each interface, we can write down the response to any given input field.

As shown in Fig. 9, we implement our model as a cascade of three components coupled to the input waveguide (I): the

absorber (II), the back-short cavity (III), and the back-short termination (IV). The air gap is not currently implemented, but could be represented by an additional component. Block III is currently modeled as enclosed in a circular waveguide with radius matching region I. Notice that this method does not require the absorber radius to match that of the waveguide – any difference can be taken up in II. Our goal is to relate the input field **A** to the reflected field **B**, and to use (1) to calculate the absorbed power.

Starting with the absorber region II and following [15], the electromagnetic fields on the left-hand-side ($\vec{E}_L$, $\vec{H}_L$) and right-hand side ($\vec{E}_R$, $\vec{H}_R$) are as follows:

$$\vec{E}_L = \sum (D_i e^{-j\beta_{Li} z} + C_i e^{j\beta_{Li} z})\vec{e}_{Li} \tag{8a}$$

$$\vec{H}_L = \sum (D_i e^{-j\beta_{Li} z} - C_i e^{j\beta_{Li} z})\vec{h}_{Li} \tag{8b}$$

$$\vec{E}_R = \sum (F_i e^{-j\beta_{Ri} z} + E_i e^{j\beta_{Ri} z})\vec{e}_{Ri} \tag{8c}$$

$$\vec{H}_R = \sum (F_i e^{-j\beta_{Ri} z} - E_i e^{j\beta_{Ri} z})\vec{h}_{Ri} \tag{8d}$$

where D_i, C_i, E_i, and F_i represent the amplitude of each waveguide mode i for signals incident upon and reflected from region II, as denoted in Fig. 9. The symbols β_{Li} and $\vec{e}_{Li}$ indicate the propagation constant and electric field on the left-hand side for mode i.

The next step is to impose the boundary conditions. Since the current in the absorber is perpendicular to the z-axis, the electric field remains continuous across the sheet while the magnetic field is discontinuous

$$\vec{E}_L = \vec{E}_R \tag{9a}$$

$$\vec{H}_L = \vec{H}_R - \frac{\vec{E}_L}{R_s} \times \hat{z} \tag{9b}$$

where R_s is the absorber sheet resistance.

We can then solve for $\mathbf{C} = (C_1, \ldots, C_i, \ldots)^T$ in terms of $\mathbf{D} = (D_1, \ldots, D_i, \ldots)^T$ and $\mathbf{E} = (E_1, \ldots, E_i, \ldots)^T$. We plug (8a) and (8c) into (9a), and right cross product with $\vec{h}^*_{Lj}$. Similarly, we plug (8b) and (8d) into (9b), and left cross product with $\vec{e}^*_{Lj}$. Finally, we integrate over the absorber surface and write everything in matrix form

$$Q(\mathbf{D} + \mathbf{C}) = S(\mathbf{F} + \mathbf{E}) \tag{10a}$$

$$P(\mathbf{D} - \mathbf{C}) = R(\mathbf{F} - \mathbf{E}) + T(\mathbf{D} + \mathbf{C}). \tag{10b}$$

Cascading with I (the input waveguide), III (the back-short cavity), and IV (the ideal back-short) as Fig. 9 indicates,

$$\mathbf{D} = X\mathbf{A} \tag{11a}$$

$$\mathbf{B} = X\mathbf{C} \tag{11b}$$

$$\mathbf{E} = W\mathbf{G} \tag{11c}$$

$$\mathbf{H} = W\mathbf{F} = -\mathbf{G} \tag{11d}$$

we find

$$\mathbf{C} = (I - Y)^{-1}(U + Y)\mathbf{D} \tag{12a}$$

$$\mathbf{B} = X(I - Y)^{-1}(U + Y)X\mathbf{A} \tag{12b}$$

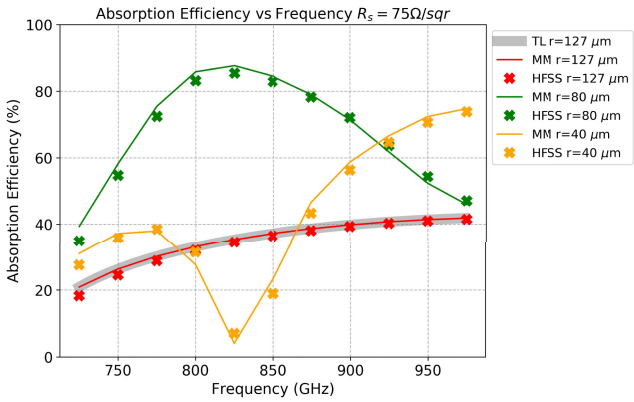

Fig. 10. Result of an absorber with mismatched sheet resistance $R_s = 75\,\Omega/\square$ and smaller radius by MM method (solid curves). Also verified by TL (grey faded curve) and HFSS (cross marks). The TL does not apply to a sheet with a radius smaller than the waveguide radius ($r_{\text{wg}} = 127\mu$m). Three different approaches result in good consistency.

where I is the identity matrix and

$$Y = V(WW - I)^{-1}WWS^{-1}Q \tag{13a}$$

$$U = (P + RS^{-1}Q + T)^{-1}(P - RS^{-1}Q - T) \tag{13b}$$

$$V = 2(P + RS^{-1}Q + T)^{-1}R. \tag{13c}$$

Explicit expressions for matrices Q, S, P, R, T, W, and X and further calculation details are relegated to the appendix.

With all of this in hand, we can compute the absorption efficiency for absorber radii less than the waveguide radius ($r \leq a$). The result (Fig. 10) shows good agreement with HFSS – the MM calculation captures the unexpected efficiency versus frequency shape at a small sheet radii. Our key observation is that a film with a very mismatched impedance (material $R_s = 1\ \Omega/\square$, effectively $75\ \Omega/\square$ with the meander filling factor) with reduced radius outperforms its waveguide-filling counterpart. At 825 GHz, for example, the smaller absorber with $r = 80\mu$m results in absorption efficiency $\sim 2.5\times$ higher than the full-radius absorber. This is informative for absorber design when sheet resistance is too low to satisfy impedance matching. Once R_s is known for a particular fabrication process, we have substantial freedom to tune the overall absorber shape to achieve good absorption efficiency at the desired frequency. Note that our unoptimized MM code does not yield computational savings for the present problem (HFSS $\sim 10^2$ s on a 32 GB RAM workstation, MM $\sim 10^3$ s on a 8 GB RAM laptop), but yields useful insights as discussed below.

With the MM method we can also understand why smaller sheets absorb more efficiently, by exploring the power in each reflected mode. We assume an input $\mathbf{A} = (1, 0, 0 \ldots)^T$, i.e., the input only has a TE_{11} component, and we consider a total of 100 modes (see the appendix for an analysis of the effect of the number of modes considered). At 850 GHz the amplitudes of the first four components for output **B** (the reflection at port 1) and **C** (the reflection at the absorber) are shown in Table I. Note that the

TABLE I
RELATIVE AMPLITUDES (NORMALIZED TO UNIT INPUT POWER) OF THE FIRST FOUR MODES OF **B** (REFLECTION AT PORT 1) AND **C** (REFLECTION AT THE ABSORBER)

	Absorber Radius (μm)	TE_{11}	TM_{11}	TE_{12}	TM_{12}
B	127	0.628	0	0	0
	80	0.155	0	0	0
C	127	0.628	0	0	0
	80	0.155	0.457	0.030	0.009

partially filled absorber excites higher order modes in **C**. These modes cannot propagate back through the input waveguide (**B** only has TE_{11} component), however, and so are confined in the vicinity of the absorber and contribute to resistive loss. Higher order modes in **C** arise from nonzero off-diagonal terms of T.

IV. CONCLUSION

Using finite-element simulations, we have demonstrated a meandered Al KID absorber for TIM with high absorption efficiency ($\sim$80%) in both x and y-polarizations. The power loss through the wafer and air gap is low ($\sim$0.1%), indicating minimal optical crosstalk between pixels. We have further developed two independent modeling tools – the TL and MM models – to better understand this high absorption efficiency given the low film resistance. These two methods will be informative for future absorber design efforts, providing intuition for how we may tune the absorber's line width, line spacing, and overall shape to maintain high efficiency for different wavelengths and film properties. Based upon the success of this design, fabrication, and testing of the first TIM test devices is anticipated in fall 2020.

Though we have demonstrated a successful design, we have several promising directions for future optimization. The MAKO-style absorber discussed here has relatively few parameters to tune (mainly meander line width and spacing), and the degree of polarization of the antenna depends upon these in nontrivial ways. The present design also relies on a relatively small air gap and a number of narrow ($\sim$0.3 μm) gaps at the mesh vertices (Fig. 1, lower right); while these parameters are manageable, a design with larger gaps and a wide tolerance in aluminum sheet resistance would be appealing. We are currently pursuing additional design efforts around an alternate absorber design that may prove more robust to fabricate for both LW and SW bands. This effort will be the subject of a future publication.

APPENDIX A
SIMULATION SETUP DETAILS

As Fig. 11 indicates, the absorber and the choke rings have impedance boundaries R_s. The vertical side surface of air gap and substrate have radiation boundaries. Other boundaries are perfect electric conductors. The mesh is length-based, with a maximum element length of 10 μm at the absorber. The overall simulation envelope has a diameter of 1623 μm and a height of 1235 μm.

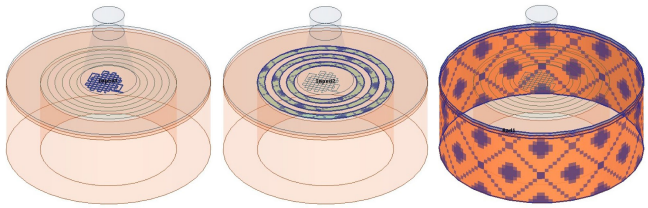

Fig. 11. Demonstration of boundary conditions. From left to right: impedance boundary R_s for absorber, impedance boundary R_s for choke rings, radiation boundaries for air gap and substrate.

APPENDIX B
MM CALCULATIONS

Matrix elements for Q, S, P, R, T, Y, W, and X

$$Q_{ij} = \int \vec{e}_{Li} \times \vec{h}^*_{Lj} dA \tag{14a}$$

$$S_{ij} = \int \vec{e}_{Ri} \times \vec{h}^*_{Lj} dA \tag{14b}$$

$$P_{ij} = \int \vec{e}^*_{Lj} \times \vec{h}_{Li} dA \tag{14c}$$

$$R_{ij} = \int \vec{e}^*_{Lj} \times \vec{h}_{Ri} dA \tag{14d}$$

$$T_{ij} = -\frac{1}{R(\rho)} \int \vec{e}^*_{Lj} \times (\vec{e}_{Li} \times \hat{z}) dA \tag{14e}$$

$$W_{ij} = \delta_{ij} e^{-j\beta_{Ri} l} \tag{14f}$$

$$X_{ij} = \delta_{ij} e^{-j\beta_{Li} d} \tag{14g}$$

where A is the waveguide cross section at $z = 0$, and l and d are the thickness of back-short and length of the input waveguide, respectively.

We choose a cylindrical coordinate system such that the z-axis is the axis of symmetry for the cylinder and points from port 1 to the back-short, and the origin is located at the center of the absorber. The $\vec{e}_i$ and $\vec{h}_i$ field thus can be written in the ρ and ϕ directions $\vec{e}_i = (e_{i\rho}, e_{i\phi})^T$, $\vec{h}_i = (h_{i\rho}, h_{i\phi})^T$. Note that $\vec{e}_i$ and $\vec{h}_i$ also depend on TE_{nm} or TM_{nm} modes. Writing this explicitly, we have [16]:

$$\vec{e}_{\mathrm{TE}i} = \begin{pmatrix} \frac{j\omega\mu n}{k_{ci}^2 \rho} \sin(n\phi) J_n(k_{ci}\rho) \\ \frac{j\omega\mu}{k_{ci}} \cos(n\phi) J'_n(k_{ci}\rho) \end{pmatrix} \equiv \begin{pmatrix} a_i \\ b_i \end{pmatrix} \tag{15a}$$

$$\vec{h}_{\mathrm{TE}i} = \begin{pmatrix} -b_i / Z_{\mathrm{TE}i} \\ a_i / Z_{\mathrm{TE}i} \end{pmatrix} \tag{15b}$$

$$\vec{e}_{\mathrm{TM}i} = \begin{pmatrix} \frac{-j\beta_i}{k_{ci}} \sin(n\phi) J'_n(k_{ci}\rho) \\ \frac{-j\beta_i n}{k_{ci}^2 \rho} \cos(n\phi) J_n(k_{ci}\rho) \end{pmatrix} \equiv \begin{pmatrix} c_i \\ d_i \end{pmatrix} \tag{15c}$$

$$\vec{h}_{\mathrm{TM}i} = \begin{pmatrix} -d_i / Z_{\mathrm{TM}i} \\ c_i / Z_{\mathrm{TM}i} \end{pmatrix} \tag{15d}$$

where

$$Z_{\mathrm{TE}i} = \omega\mu / \beta_i \tag{16a}$$

$$Z_{\mathrm{TM}i} = \beta_i/\omega\epsilon. \tag{16b}$$

Before moving forward, we first clarify what assumptions have been made. This study (1) contains a circular absorber with uniform sheet resistance, such that $R(\rho \le r) = R_s, R(\rho > r) = \infty$, and (2) the input to the waveguide consists only of the first mode, TE_{11}. It is important to note that the MM can analyze a system without these two assumptions, at the cost of additional algebraic complexity. For general waveguide modes, $e_{i\rho}$, $e_{i\phi}$, $h_{i\rho}$, and $h_{i\phi}$ have both sin and cos terms. Due to our single-moded input, however, we can always rotate the coordinate system around the z-axis so that one term is zero. Here, we choose nonzero sin term for $e_{\mathrm{TE}i\rho}$. Furthermore, by rotational symmetry, the higher excited $e_{i\rho}$ and $h_{i\rho}$ have only sin terms and the higher excited $e_{i\phi}$ and $h_{i\phi}$ have only cos terms. (Cross terms go to zero after $\int_0^{2\pi} d\phi$). In addition, recalling the notation TE_{nm} and TM_{nm}, modes with $n \neq 1$ vanish after integration. We can thus plug $n = 1$ into (15) to simplify our calculation. Finally, note that the cutoff frequency k_c, the propagation constant β, and the impedance Z depend on mode number and TE/TM character; the latter two can also differ on the two sides of each interface, since waveguide and back-short have different material ϵ.

Note that in this study we have used a single index i to denote any waveguide mode $\mathrm{TE/TM}_{nm}$. The one-to-one map between the two sets of indices is as follows:

1) Based on cutoff frequency, from low to high, list the corresponding mode number. (TE_{11}, TM_{01}, TE_{21}, TM_{11}, ...)
2) Use the identity $\forall\, n, m \in \mathbb{Z}^+, \int_0^{2\pi} \sin(nx)\sin(mx)dx = \delta_{nm}\pi$. The input mode TE_{11} only excites nonzero terms for TE_{1m} and TM_{1m}. From previous mode set remove zero terms. (TE_{11}, TM_{11}, TE_{12}, TM_{12}, ...)
3) Choose the total number of modes – e.g., 10. Rearrange the mode set such that TE or TM are collected together. (TE_{11}, ..., TE_{15}, TM_{11}, ..., TM_{15})
4) Label the mode set from the previous step as modes (1, ..., i, ..., 10).

With this mode order construction, any element from (14) ends up with one of four different corners in its matrix

$$\left(\begin{array}{c|c} \mathrm{TE}\times\mathrm{TE} & \mathrm{TE}\times\mathrm{TM} \\ \hline \mathrm{TM}\times\mathrm{TE} & \mathrm{TM}\times\mathrm{TM} \end{array}\right)$$

and we have the following full expression for matrix elements before integration:

$$Q_{ij}: \begin{cases} (a_{Li}a^*_{Lj} + b_{Li}b^*_{Lj})/Z^*_{\mathrm{TE}Lj} & (\mathrm{TE}\times\mathrm{TE}) \\ (a_{Li}c^*_{Lj} + b_{Li}d^*_{Lj})/Z^*_{\mathrm{TM}Lj} & (\mathrm{TE}\times\mathrm{TM}) \\ (c_{Li}a^*_{Lj} + d_{Li}b^*_{Lj})/Z^*_{\mathrm{TE}Lj} & (\mathrm{TM}\times\mathrm{TE}) \\ (c_{Li}c^*_{Lj} + d_{Li}d^*_{Lj})/Z^*_{\mathrm{TM}Lj} & (\mathrm{TM}\times\mathrm{TM}) \end{cases} \tag{17a}$$

$$S_{ij}: \begin{cases} (a_{Ri}a^*_{Lj} + b_{Ri}b^*_{Lj})/Z^*_{\mathrm{TE}Lj} & (\mathrm{TE}\times\mathrm{TE}) \\ (a_{Ri}c^*_{Lj} + b_{Ri}d^*_{Lj})/Z^*_{\mathrm{TM}Lj} & (\mathrm{TE}\times\mathrm{TM}) \\ (c_{Ri}a^*_{Lj} + d_{Ri}b^*_{Lj})/Z^*_{\mathrm{TE}Lj} & (\mathrm{TM}\times\mathrm{TE}) \\ (c_{Ri}c^*_{Lj} + d_{Ri}d^*_{Lj})/Z^*_{\mathrm{TM}Lj} & (\mathrm{TM}\times\mathrm{TM}) \end{cases} \tag{17b}$$

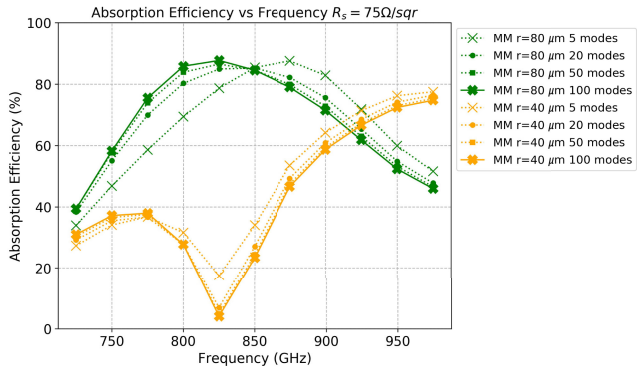

Fig. 12. Comparison of MM solutions computed with different numbers of modes, indicating that 100 modes is adequate for convergence.

$$P_{ij}: \begin{cases} (a_{Li}a^*_{Lj} + b_{Li}b^*_{Lj})/Z_{\mathrm{TE}Li} & (\mathrm{TE}\times\mathrm{TE}) \\ (a_{Li}c^*_{Lj} + b_{Li}d^*_{Lj})/Z_{\mathrm{TE}Li} & (\mathrm{TE}\times\mathrm{TM}) \\ (c_{Li}a^*_{Lj} + d_{Li}b^*_{Lj})/Z_{\mathrm{TM}Li} & (\mathrm{TM}\times\mathrm{TE}) \\ (c_{Li}c^*_{Lj} + d_{Li}d^*_{Lj})/Z_{\mathrm{TM}Li} & (\mathrm{TM}\times\mathrm{TM}) \end{cases} \tag{17c}$$

$$R_{ij}: \begin{cases} (a_{Ri}a^*_{Lj} + b_{Ri}b^*_{Lj})/Z_{\mathrm{TE}Ri} & (\mathrm{TE}\times\mathrm{TE}) \\ (a_{Ri}c^*_{Lj} + b_{Ri}d^*_{Lj})/Z_{\mathrm{TE}Ri} & (\mathrm{TE}\times\mathrm{TM}) \\ (c_{Ri}a^*_{Lj} + d_{Ri}b^*_{Lj})/Z_{\mathrm{TM}Ri} & (\mathrm{TM}\times\mathrm{TE}) \\ (c_{Ri}c^*_{Lj} + d_{Ri}d^*_{Lj})/Z_{\mathrm{TM}Ri} & (\mathrm{TM}\times\mathrm{TM}) \end{cases} \tag{17d}$$

$$T_{ij}: \begin{cases} (a_{Li}a^*_{Lj} + b_{Li}b^*_{Lj})/R_s & (\mathrm{TE}\times\mathrm{TE}) \\ (a_{Li}c^*_{Lj} + b_{Li}d^*_{Lj})/R_s & (\mathrm{TE}\times\mathrm{TM}) \\ (c_{Li}a^*_{Lj} + d_{Li}b^*_{Lj})/R_s & (\mathrm{TM}\times\mathrm{TE}) \\ (c_{Li}c^*_{Lj} + d_{Li}d^*_{Lj})/R_s & (\mathrm{TM}\times\mathrm{TM}) \end{cases}. \tag{17e}$$

We need to consider the normalization factor before calculating each element. The first thing we notice is the orthogonality between modes. Since Q, S, P, and R all integrate through entire waveguide cross section, only diagonal terms are nonzero. They can be calculated analytically based on the following identity:

$$\int_0^{p'_i} \left(J'_v(x)^2 + \frac{v^2}{x^2}J_v(x)^2\right) x dx = (p'^2_i - v^2)\frac{J_v(p'_i)^2}{2} \tag{18a}$$

$$\int_0^{p_i} \left(J'_v(x)^2 + \frac{v^2}{x^2}J_v(x)^2\right) x dx = p_i^2\frac{J'_v(p_i)^2}{2} \tag{18b}$$

where $J_v(p_i) = 0$ and $J'_v(p'_i) = 0$.

The T elements integrate over the absorber surface and provide off-diagonal terms in our calculation. They have to be calculated numerically. Physically, this represents the nonzero crosstalk between different modes.

In this study, the total number of modes we implement in MM calculation is 100. Fig. 12 shows comparison between number of modes. The results are converged with increasing the total number of modes.

ACKNOWLEDGMENT

The authors would like to thank C. McKenney and T. Reck for their useful scientific discussions.

REFERENCES

[1] M. G. Hauser and E. Dwek, "The cosmic infrared background: Measurements and implications," *Annu. Rev. Astron. Astrophys.*, vol. 39, pp. 249–307, Jan. 2001, doi: 10.1146/annurev.astro.39.1.249.

[2] G. Lagache, J.-L. Puget, and H. Dole, "Dusty infrared galaxies: Sources of the cosmic infrared background," *Annu. Rev. Astron. Astrophys.*, vol. 43, no. 1, pp. 727–768, Sep. 2005, doi: 10.1146/annurev.astro.43.072103.150606.

[3] E. D. Kovetz *et al.*, "Line-intensity mapping: 2017 status report," Sep. 2017. [Online]. Available: https://arxiv.org/abs/1709.09066

[4] E. Kovetz *et al.*, "Astrophysics and cosmology with line-intensity mapping," *Bull. Amer. Astronomical Soc.*, vol. 51, no. 3, May 2019, Art. no. 101. [Online]. Available: https://arxiv.org/abs/1903.04496

[5] J. Vieira *et al.*, "The Terahertz intensity mapper (tim): An imaging spectrometer for galaxy evolution studies at high-redshift," in *Proc. Int. Symp. Space THz Technol.*, Gothenburg, Sweden, Jun. 2019, pp. 208–215. [Online]. Available: https://www.nrao.edu/meetings/isstt/papers/2019/2019208215.pdf

[6] M. Meixner, *et al.* "Origins space telescope mission concept study report," Dec. 2019, *arxiv.1912.06213v2*.

[7] S. Hailey-Dunsheath *et al.* , "Development of aluminum LEKIDs for balloon-borne far-IR spectroscopy," *J. Low Temp. Phys.*, vol. 193, no. 5/6, pp. 968–975, Dec. 2018, doi: 10.1007/s10909-018-1927-y.

[8] C. M. McKenney *et al.*, "Design considerations for a background limited 350 micron pixel array using lumped element superconducting microresonators," *Proc.SPIE*, vol. 8452, pp. 220–229, 2012, doi: 10.1117/12.925759.

[9] J. Hubmayr *et al.*, "Photon-noise limited sensitivity in titanium nitride kinetic inductance detectors," *Appl. Phys. Lett.*, vol. 106, no. 7, Feb. 2015, Art. no. 073505.

[10] S. Hailey-Dunsheath *et al.*, "Low noise titanium nitride KIDs for SuperSpec: A millimeter-wave on-chip spectrometer," *J. Low Temp. Phys.*, vol. 184, no. 1/2, pp. 180–187, Jul. 2016.

[11] R. McGeehan *et al.*, "Low-temperature noise performance of SuperSpec and other developments on the path to deployment," *J. Low Temp. Phys.*, vol. 193, pp. 1024–1032, Sep. 2018.

[12] J. Bueno *et al.*, "Anomalous response of superconducting titanium nitride resonators to Terahertz radiation," *Appl. Phys. Lett.*, vol. 105, no. 19, Nov. 2014, Art. no. 192601.

[13] P. J. de Visser, J. J. A. Baselmans, J. Bueno, N. Llombart, and T. M. Klapwijk, "Fluctuations in the electron system of a superconductor exposed to a photon flux," *Nature Commun.*, vol. 5, Feb. 2014, Art. no. 3130.

[14] M. Rosch, "Development of lumped element kinetic inductance detectors for mm-wave astronomy at the IRAM 30 m telescope," Ph.D. dissertation, Karlsruher Institut for Technologie, Fakultät für Elektrotechnik und Informationstechnik, Karlsruhe, Germany, Jun. 2013.

[15] S. Doherty, "Optical and quasi-optical design and analysis of astronomical instrumentation including a prototype safari pixel," Ph.D. dissertation, Dept. Exp. Phys., Maynooth Univ., Maynooth, Ireland, Oct. 2012. [Online]. Available: http://mural.maynoothuniversity.ie/3999/

[16] D. M. Pozar, *Microwave Engineering*. Hoboken, NJ, USA: Wiley, Mar. 2011.